

Shear deformation, ideal strength, and stacking fault formation of fcc metals: A density-functional study of Al and Cu

Michal Jahnátek,^{1,*} Jürgen Hafner,^{1,†} and Marián Krajčí^{1,2,‡}

¹*Faculty of Physics and Center for Computational Materials Science, University of Vienna, Sensengasse 8/12, A-1090 Vienna, Austria*

²*Institute of Physics, Slovak Academy of Sciences, Dúbravská cesta 9, SK-84511 Bratislava, Slovakia*

(Received 19 March 2009; revised manuscript received 23 April 2009; published 4 June 2009)

Ab initio density-functional calculations have been used to study the response of two face-centered-cubic metals (Al and Cu) to shearing parallel to the close-packed (111) planes along two different directions, $[11\bar{2}]$ and $[\bar{1}10]$. Two different types of deformations—affine and alias—have been investigated. Under an affine shear deformation, all atoms are shifted parallel to the shearing direction by a distance proportional to their distance from the fixed basal plane. In the alias regime, only the top layer is displaced in the shearing direction. In both regimes, calculations have been performed with (pure shear) and without (simple shear) relaxation. For a pure alias shear, due to the interaction between the atoms, the displacement propagates through the sample; this is certainly the most realistic description of the shearing processes. In the pure alias regime, shear deformation, theoretical shear strength, and stacking fault formations may be described on a common footing. For small strains (in the elastic region), affine and alias shears lead to very similar results. Beyond the elastic limit, relaxation has a strong influence of the response on an applied shear strain. The elastic shear moduli are significantly larger for Cu than for Al, but a much higher shear strength is calculated for Al, although the shear strength is limited by the occurrence of a stacking fault instability before the stress maximum is reached. Under $\langle\bar{1}10\rangle\{111\}$ shear the analysis of the atomistic deformation mechanism shows that in this case the formation of a stacking fault leads to a splitting of the $\frac{1}{2}[\bar{1}10]$ dislocation into two partial Shockley dislocations. Due to the repulsive interaction between the atoms in adjacent close-packed planes, the atoms in the top A layer move along $\frac{1}{6}[\bar{2}11]$ to a position directly above the B layer such that the stable intrinsic stacking fault configuration is the same for both slip systems. The analysis of the variation in the lattice parameters under strain reveals significant differences in the relaxation behavior of both metals: Al is very stiff, but Cu is rather soft along the $\langle112\rangle$; in-plane relaxation is very strong for Cu but modest for Al. This much stronger relaxation explains that while the differences in the unstable stacking fault energies of both metals are only modest, the intrinsic stacking fault energies differ by as much as a factor of 4. A detailed comparison of the response to shear and tensile deformations has been performed. A phonon instability of the uniaxial tensile deformation along the $[110]$ direction has been explained by the close connection with the shear system $\langle11\bar{2}\rangle\{111\}$.

DOI: [10.1103/PhysRevB.79.224103](https://doi.org/10.1103/PhysRevB.79.224103)

PACS number(s): 62.20.F-, 61.72.Nn, 62.25.-g

I. INTRODUCTION

High strength and good ductility are the most important properties of metallic structural materials. The strength of a material is determined by the maximum stress that the material can sustain. If this critical stress is exceeded the material fails either by fracture or by yielding. For real materials the strength is controlled by the formation and propagation of line defects (dislocations) or microcracks. The movement of dislocations controls the plastic deformation of the material; the propagation of cracks leads to brittle fracture.¹ The ideal or theoretical strength can be reached only in a perfect single crystal free of any defects; it is determined solely by the chemical binding forces holding the atoms together. The value of the ideal strength depends on the type of deformation (tension or shear) and the direction of the applied strain. Theoretically the value of the ideal shear strength (ISS) is related to the stress necessary for the nucleation of a dislocation and for the formation of stacking faults (SFs). The value of the ideal tensile strength (ITS) is determined by the local stress required for the generation and propagation of a microcrack. Hence, since plastic deformation is controlled by the nucleation and propagation of dislocations,² while brittle

cleavage is initiated by crack formation, the ratio of the ideal tensile and shear strengths can be used to characterize the ductility or brittleness of a material.^{1,3}

A model of an edge dislocation can be produced by removing from the crystal half a lattice plane terminating at the dislocation line and carefully joining back together the two planes on either side of the missing plane such that the perfect crystal lattice is disturbed only in the vicinity of the dislocation. A screw dislocation can be constructed by choosing a lattice plane terminating at the dislocation line, displacing the upper part of the crystal by a lattice vector parallel to the line, and joining it again to the lower part of the crystal such that the crystalline structure is restored everywhere except close to the dislocation line. A dislocation is characterized by the dislocation-displacement vector \vec{b} (or Burgers vector) defined as follows: (i) construct a closed path defined by a series of lattice vectors in a perfect dislocation-free region. (ii) Go through the same series of lattice vectors in a region where a line defect could exist. If the path fails to reconnect to the starting point, it surrounds a dislocation. The lattice vector connecting end and starting points of the path is the Burgers vector \vec{b} of the dislocation. The Burgers vector is perpendicular to the dislocation line for an edge dislocation.

tion and parallel for a screw dislocation. A shear deformation where a lattice plane glides over another can be produced by one or more dislocations. A particular shear deformation is described by the definition of the glide plane and the direction of the deformation. E.g., the $\langle 11\bar{2} \rangle \{111\}$ shear system in a face-centered-cubic lattice describes a relative displacement of two close-packed $\{111\}$ planes along the $\langle 11\bar{2} \rangle$ direction. For each lattice type there exist a number of experimentally observed slip systems characteristic for the crystal symmetry.

The results of all investigations consistently indicate that a $\langle 110 \rangle \{111\}$ shear deformation is the major operative slip system for face-centered-cubic (fcc) structures.⁴ The smallest possible dislocation generated by this shear deformation is described by the Burgers vector $\vec{b} = \frac{1}{2}\langle 110 \rangle$. However, the formation of a dislocation with this Burgers vector may be prevented by the splitting of the dislocation into two partial Shockley dislocations which is favored by the presence of a stacking fault with a lower misfit energy.⁴ The ideal fcc lattice consists of a ...ABCABCABC... stacking sequence of close-packed $\{111\}$ planes [see Fig. 1(a)], and a $\langle 110 \rangle \{111\}$ slip is realized by moving top layer A over layer C along the $[\bar{1}10]$ direction, as sketched in Fig. 1(b). A shift of the atoms in top layer A over the atoms in the C layer along this direction leads to a steeper increase in the energy than if the A atoms are shifted first to the B positions. This can be written as a splitting of the Burgers vector according to $\frac{1}{2}[\bar{1}10] \rightarrow \frac{1}{6}[\bar{2}11] + \frac{1}{6}[\bar{1}2\bar{1}]$. The dislocation displacement of type $\frac{1}{6}\langle 112 \rangle$ is called a Shockley partial and is glissile on the (111) plane. Such a displacement between layers C and A leads into a local ...ABC|BCA... stacking sequence with a SF marked as |. The stacking fault is surrounded by layers stacked in the same sequence as in a hexagonal-close-packed (hcp) structure (...BCBC...).⁵ Partial dislocations are important in twinning reactions which are the predominant deformation mechanism of fcc metals and alloys with a low stacking fault energy (SFE),⁶ e.g., Cu.⁷ However, recently also experimental observations of partial Shockley dislocations in nanocrystalline fcc metals with a high SFE [e.g., Al (Refs. 8 and 9) or Pd (Ref. 10)] have been reported. Partial dislocations are also important barriers to dislocation motion.⁴

In this paper we present *ab initio* density-functional calculations of the ideal shear strength in fcc metals during (111) shear deformations in connection with possible stacking faults effects. In the past different methods have been used for the determination of the ideal strength and for the calculation of stacking fault energies and the investigation of dislocation motions. The IS has been calculated by applying an affine shear strain to the crystalline lattice,^{11–16} whereas dislocation studies been based on a supercell approach where two parts of the cell are displaced against each other^{14,17–21} leading directly to the calculation of generalized stacking fault energy (GSFE) curves.^{22,23} Both concepts have been used in our study, leading to a unified view of shear strength, stacking fault energies, and dislocations movement. A similar synthesis has also been attempted by Finkenstadt and Johnson.²⁴

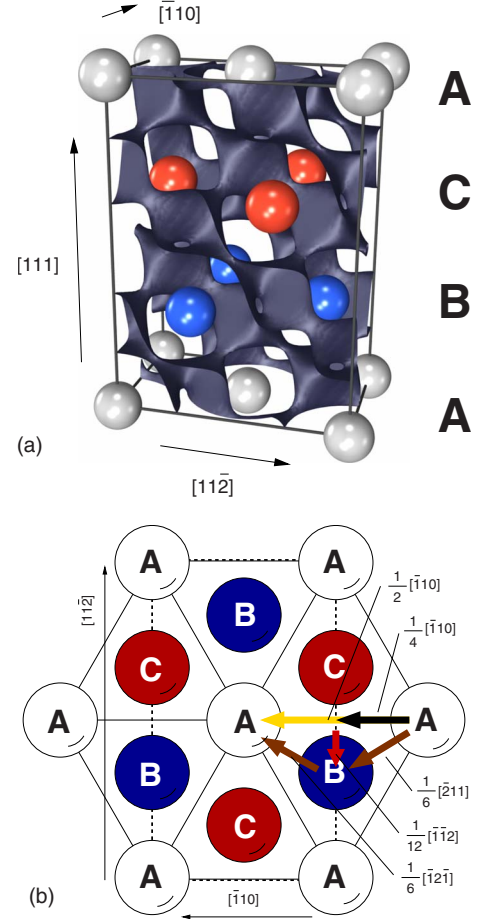


FIG. 1. (Color online) (a) The geometry of the computational cell used for the investigation of $\langle 11\bar{2} \rangle \{111\}$ and $\langle \bar{1}10 \rangle \{111\}$ shear deformations of fcc metals. The three lattice vectors spanning the cell are parallel to the $[11\bar{2}]$, $[\bar{1}10]$, and $[111]$ directions of the fcc unit cell. Atoms within this cell occupy three close-packed planes labeled as A, B, and C. The isosurface of the difference charge density as calculated for Al is shown for a density of $18 \times 10^{-3} \text{ e}/\text{\AA}^3$. (b) The smallest possible perfect dislocation $\frac{1}{2}[\bar{1}10]$ is split into two partial Shockley dislocations $\frac{1}{6}[\bar{2}11] + \frac{1}{6}[\bar{1}2\bar{1}]$ because a stacking fault leads to a lower misfit energy. This state is called as an intrinsic stacking fault configuration (ISFC) located at the $\frac{1}{12}[\bar{1}\bar{1}2] + \frac{1}{6}[\bar{1}2\bar{1}]$ position, what is associated with the spitting mechanism of the half-perfect dislocation $\frac{1}{4}[\bar{1}10]$.

II. COMPUTATIONAL METHODOLOGY

Our *ab initio* total-energy and force calculations are based on density-functional theory (DFT) as implemented in the Vienna *ab initio* simulation package (VASP).^{25,26} A gradient-corrected functional has been used to describe electronic exchange and correlations.²⁷ Electron-ion interactions are treated within the projector-augmented-wave (PAW) method.^{28,29} For both elements we used the standard PAW pseudopotentials (PP) distributed with VASP with reference configurations $_{13}\text{Al}:[\text{Ne}]3s^23p^1$ and $_{29}\text{Cu}:[\text{Ar}]3d^{10}4s^1$. The plane-wave basis set contained components with kinetic energies up to 350 eV. The lattice parameter a , the elastic constants C_{ij} , and the shear moduli relating stress and strain

TABLE I. Lattice parameter a , elastic constants C_{ij} , and shear modulus G for face-centered-cubic Al and Cu, compared with experiment (Refs. 32 and 33). G_u and G_r stand for the unrelaxed ($\epsilon_{ij}=0$ except ϵ_{13} or ϵ_{23}) and the relaxed ($\sigma_{ij}=0$ except σ_{13} or σ_{23}) shear constants (see Ref. 30). Superscripts 112 and 110 denote the relation to the $\langle 112 \rangle \{111\}$ and $\langle 110 \rangle \{111\}$ shear deformations, respectively. All elastic constants and shear moduli are presented in GPa units.

		a [Å]	C_{11}	C_{12}	C_{44}	G_u^{112}	G_r^{112}	G_u^{110}	G_r^{110}
Al	Theor.	4.046	111	56	32	29.2	29.1	30.7	30.5
	Exp.	4.045	108	62	28	24.7	24.5	26.5	26.3
Cu	Theor.	3.632	180	120	84	47.9	38.0	66.0	52.4
	Exp.	3.616	177	125	81	44.4	33.5	62.9	47.5

along the $[11\bar{2}]$ and $[\bar{1}10]$ directions in the (111) plane calculated with these potentials for both metals are collected in Table I. The shear moduli are defined as

$$G_u^{112} = C'_{55} = \frac{1}{3}(C_{11} - C_{12} + C_{44}), \quad (1)$$

$$G_r^{112} = \frac{1}{S'_{55}} = \frac{3C_{44}(C_{11} - C_{12})}{4C_{44} + C_{11} - C_{12}}, \quad (2)$$

for the $\langle 11\bar{2} \rangle \{111\}$ shear system^{11,30,31} and

$$G_u^{110} = C'_{44} = \frac{1}{6}(C_{11} - C_{12} + 4C_{44}), \quad (3)$$

$$G_r^{110} = \frac{1}{S'_{44}} = \frac{3C_{44}(C_{11} - C_{12})}{2(C_{44} + C_{11} - C_{12})}, \quad (4)$$

for the $\langle \bar{1}10 \rangle \{111\}$ shear system. The good agreement between theory and experiment shows that a gradient-corrected functional, combined with the all-electron PAW methods, yields a very accurate description of the structural and elastic properties.

The Brillouin zone (BZ) was sampled using a $21 \times 35 \times 15$ and $12 \times 17 \times 7$ mesh for Al and Cu, respectively, constructed according to the Monkhorst-Pack scheme.³⁴ The integration over the BZ used the Methfessel-Paxton smearing method with 0.3 eV smearing width³⁵ or the tetrahedron method with Blöchl corrections.³⁶ The total energy was calculated with a high precision, converged to 10^{-6} eV/atom.

The basal plane of the orthorhombic computational cell is parallel to the (111) plane of the fcc structure; the \vec{a} and \vec{b} lattice vectors are parallel to the $[11\bar{2}]$ and $[\bar{1}10]$ directions of the fcc lattice, respectively. The lattice vector \vec{c} is perpendicular to this plane and parallel to the $[111]$ direction. The cell contains six atoms on three close-packed planes, arranged in a $-ABC-$ stacking sequence (see Fig. 1). This computational cell has been used for studying both the $\langle 11\bar{2} \rangle \{111\}$ and the $\langle \bar{1}10 \rangle \{111\}$ slip systems.

Using this cell we investigated the response of the material to shear deformations by applying two different types of deformation: affine and alias. For an affine shear transformation all atoms are shifted parallel to the direction of shearing by a distance proportional to their perpendicular distance

from the fixed basal plane [see Fig. 2(a)]. The affine shear transformation preserves horizontal lines and parallelism (parallel lines are mapped onto parallel lines). The affine shear deformation changes only the lattice vectors, while the fractional coordinates of the atomic positions within the cell remain unchanged.

For an alias shear deformation only the top layer of the cell is displaced in the shear direction, while the atoms in all other layers remain in their original positions [see Fig. 2(b)]. The designation as ‘‘alias shear’’ is derived from the alias transformation in which the coordinate system is changed,

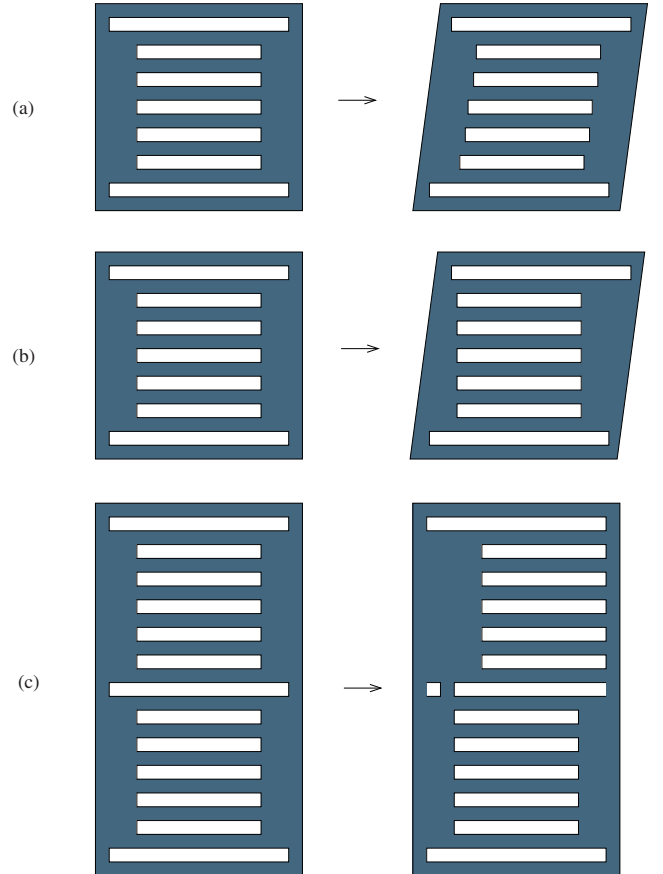


FIG. 2. (Color online) The schematic view of possible deformation regimes: (a) the affine shear, (b) the alias shear, and (c) the regime used commonly for the calculation of GSF E curves-slab regime.

leaving vectors in the original coordinate system “fixed” while changing their representation in the new coordinate system. This type of deformation assumes that all atomic positions are represented in the same coordinate system as the lattice vectors (Cartesian coordinate system). The resulting structure differs from that produced by an affine shear deformation. The displacement of the top layer at first influences only the next layer, but a relaxation at a fixed displacement of the upper layer leads to a propagation of the displacement from top \rightarrow down. In some sense this leads to a more realistic description of the deformation mechanism than the affine shear deformation. In particular, this mechanism also permits generation of stacking faults. A similar type of deformation is commonly used nowadays in theoretical investigations of the nucleation of dislocations. The energy-displacement curves, known as GSFE curves, are often calculated by a relative displacement of two slabs of the crystal in opposite directions, while relaxation processes are allowed only along the normal vector of the gliding plane. Figure 2(c) illustrates this type of deformation which is entirely analogous to the alias deformation shown in Fig. 2(b).

A quasireversible deformation process at zero absolute temperature was assumed for all types of deformation. For both affine and alias shear deformations we considered two modes of shearing, as defined by Ogata *et al.*,¹⁴ pure and simple shear. Simple shear means that the shear deformation is not followed by a relaxation of the shape of the sheared cell and the positions of the atoms. Pure shear implies a full relaxation of the cell (shape and atomic coordinates), with the only constraint that the shearing angle is fixed; i.e., all components of the stress tensor σ_{ij} except σ_{13} or σ_{23} have to vanish after relaxation for the $\langle 11\bar{2} \rangle \{111\}$ or $\langle \bar{1}10 \rangle \{111\}$ shear systems, respectively. Relaxation has been performed using the external optimizer GADGET developed by Bučko *et al.*,³⁷ which allows the use of symmetry-adapted generalized coordinates. The forces acting on the atoms were computed via the Hellmann-Feynman theorem;³⁸ the stress tensor acting on the unit cell was computed via the generalized virial theorem.^{39,40} The structural relaxation was stopped when all forces acting on the atoms were converged to within 10^{-3} eV/Å and all components of the stress tensor (except σ_{13} or σ_{23}) were converged to within 0.05 GPa (note that this is much smaller than the size of a data point in the stress-strain curves).

At each step of a pure shear deformation, the configuration of the previous step was used as a starting point. Here, an important point is the increment by which the displacement is increased in succeeding steps. For $\langle 11\bar{2} \rangle \{111\}$ shear deformation the increment in the displacement was in general 2.5%, but in all cases we have used a much smaller increment of 1% around the unstable stacking fault configuration (USFC) in order to locate the occurrence of the stacking fault instability very precisely. A very small increment of the displacement has also been used for simple alias shear under $\langle 11\bar{2} \rangle \{111\}$ shear deformation for Cu (see Fig. 3) and for pure alias shear of both metals under a $\langle \bar{1}10 \rangle \{111\}$ shear deformation (see Fig. 8).

III. RESULTS

The main results of our investigation can be cast into the form of energy- and stress-displacement curves. These are shown in Figs. 3 and 8 for the two different slip systems, $\langle 11\bar{2} \rangle \{111\}$ and $\langle \bar{1}10 \rangle \{111\}$, respectively. Each figure shows a set of four curves corresponding to simple and pure shear modes for affine and alias deformations. As measure of the shear deformation we have chosen the value of the displacement of the top layer relative to the bottom layer of the computational cell. We find that this is more intuitive than a representation in terms of the engineering shear strain for which there is no unique definition at finite strain.¹¹ The displacement is given as $(|\vec{x}|/|\vec{b}|)100\%$, where \vec{x} is the displacement of the end point of lattice vector \vec{c} along the Burgers vector \vec{b} . We will distinguish between two displacements, μ and ξ , associated with the displacement along the $\vec{b} \equiv \vec{b}^{\langle 11\bar{2} \rangle} = [11\bar{2}]a_0$ and $\vec{b} \equiv \vec{b}^{\langle \bar{1}10 \rangle} = [\bar{1}10]a_0$, respectively, where a_0 stands for the equilibrium lattice constant of the fcc structure.

In dislocation theory, the deformation is usually measured in fractions of the partial Burgers vector $\vec{b}_p \equiv \vec{b}^{\langle 11\bar{2} \rangle} = \frac{1}{6}\vec{b}^{\langle 11\bar{2} \rangle}$ or $\vec{b}_p \equiv \vec{b}_p^{\langle \bar{1}10 \rangle} = \frac{1}{2}\vec{b}^{\langle \bar{1}10 \rangle}$. With these definitions the basal lattice vectors of the computational cell can be expressed as $\vec{a}_{\text{(lattice)}} = \frac{1}{2}\vec{b}^{\langle 11\bar{2} \rangle} = 3\vec{b}_p^{\langle 11\bar{2} \rangle}$ and $\vec{b}_{\text{(lattice)}} = \frac{1}{2}\vec{b}^{\langle \bar{1}10 \rangle} = 2\vec{b}_p^{\langle \bar{1}10 \rangle}$. This alternative scale is shown on the top of graphs. Deformation energies are given both in meV/atom (left-hand scale) and in units of mJ/m² as usual for the GSFE defined as $\gamma(\vec{x}) = E(\vec{x})/S_0$, where S_0 is surface of the basal plane of the undeformed cell (as shown on the right side of graphs). If a relaxation of the cell shape is permitted, the area of the basal plane might be slightly changed. However, corrections to the stacking fault energies are always smaller than 2%.

A. $\langle 11\bar{2} \rangle \{111\}$ slip system

1. Energy- and stress-displacement curves

The energy- and the stress-displacement curves for Al and Cu under $\langle 11\bar{2} \rangle \{111\}$ shear deformation are presented in Fig. 3. In the elastic limit (up to 1%) the results obtained with the different modes of shear deformation are indistinguishable. Except simple alias shear, the remaining three deformations produce identical results of up to $\sim 10\%$ and $\sim 5\%$ displacements for Al and Cu, respectively. It is remarkable that a simple (unrelaxed) affine shear deformation yields correct results up to these limits. Pure (relaxed) affine and alias shear deformations lead to almost identical energies and stresses of up to $\sim 20\%$ and $\sim 25\%$ displacements for Al and Cu, respectively.

Beyond this limit, the response to affine and alias deformations is substantially different. While under an affine shear deformation the stress continues to increase monotonously, pure alias shear deformation leads to the generation of a SF. This is not surprising since stacking fault generation consists in a displacement of two neighboring layers in opposite directions. This is possible in the alias regime but suppressed by definition in the affine shear regime. A comparison of

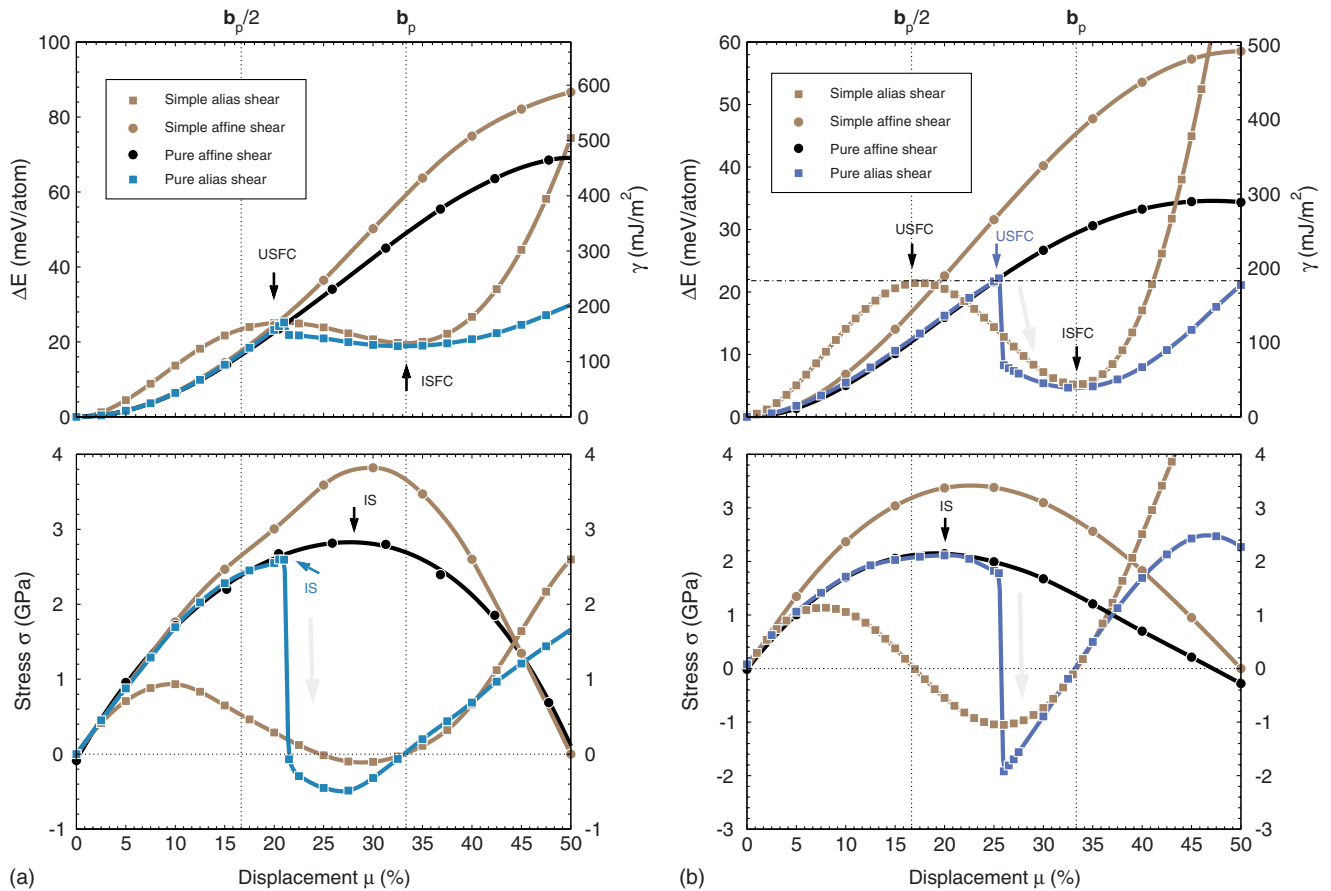


FIG. 3. (Color online) Energy- and stress-displacement curves under a $\langle 11\bar{2} \rangle \{111\}$ shear deformation in Al (left) and Cu (right) for different modes of deformation. The labels IS, ISFC, and USFC, mark the displacement, energy, and shear stress for ideal strength, intrinsic, and unstable stacking fault configurations, respectively. The essential difference in the response of Al and Cu to a shear deformation is that the value of the IS (determined by an affine shear deformation) is reached before generation of a stacking fault (by an alias shear deformation) for Cu but not for Al.

simple and pure shear deformations allows assessment of the importance of relaxation processes. Under affine shear deformation, relaxation effects are modest up to $\sim 12.5\%$ and $\sim 5\%$ displacements for Al and Cu, respectively. Hence relaxation processes are much more important for Cu, and the difference is also illustrative of different relaxation mechanisms.^{14,31} In contrast, for alias shear deformation, relaxation is very important even in the elastic region.

The deformation curve calculated for simple alias shear is closely related to the GSFE curves. The first energy maximum determines the so-called unstable stacking fault energy (USFE) γ_{USF} , which represents the energy barrier for the generation of a stacking fault. The first energy minimum defines the intrinsic (stable) stacking fault energy (ISFE). The USFE under $\langle 11\bar{2} \rangle \{111\}$ shear deformation also represents the lowest energy barrier for dislocation nucleation, while under $\langle 110 \rangle \{111\}$ shear at the displacement corresponding to the intrinsic stacking fault the dislocation dissociates into a pair of Shockley partials.⁴⁶ The calculated stacking fault energies are collected in Table II and are compared to previous results. We note that available values scatter appreciably, depending on the exchange-correlation functional and the description of the electron-ion interaction. For Al the wide scatter is partially a consequence of the well-known poor

convergence of total energy of Al with the number of \vec{k} points in the BZ. This is not the case for Cu, where the total energy can be computed accurately with relatively sparse \vec{k} -point meshes. Agreement is best with recently published results of Kibey *et al.*^{6,42} which were obtained with a comparable method. The wide scatter of the experimental stacking fault energies for Al reflects the difficulty in resolving the Shockley partial dislocations.

For simple alias shear applied to Cu the displacement vectors associated with the γ_{ISF} and γ_{USF} configurations are given by $\frac{1}{6}[11\bar{2}] = \vec{b}_p$ and $\frac{1}{12}[11\bar{2}] = \frac{1}{2}\vec{b}_p$, respectively. For Al the situation is different. The ISFC is of course again given by the partial Burgers vector \vec{b}_p , but the USFC is found at a substantially larger displacement and—also in contrast to Cu—the stress-strain curve is strongly asymmetric. The high degree of symmetry observed for Cu results from a short-range interaction, only the relative displacement of the two top layers is important. For Al the displacement dependence of energy and strain is modified by long-range interactions between the layers. Similar results have also been reported by Ogata *et al.*¹⁴ If the system is allowed to relax (“pure” shear) for Cu a larger displacement is possible before reaching the unstable stacking fault configuration [see Figs. 3(a) and 3(b)], while the displacement for the intrinsic stacking

TABLE II. Unstable and intrinsic stacking fault energies (in mJ/m^2) of Al and Cu for $\langle 11\bar{2} \rangle \{111\}$ shear deformation, calculated for simple and pure alias shear deformation. More data for comparison can be found in Ref. 41.

Data source		Al		Cu	
		γ_{USF}	γ_{ISF}	γ_{USF}	γ_{ISF}
This work	Simple alias shear	169	134	180	41
	Pure alias shear	169	126	186	37
Others	(GGA-PAW) ^b	162	130	180	41
	(GGA-PAW) ^d	178	146	164	38
	(GGA-US) ^c	175	158	158	39
	(GGA-PAW) ^f	181	41
	(LDA-US) ^a	...	134
	(GGA-US) ^a	...	124
	(GGA-PAW) ^a	...	122
	(LDA) ^e	174	133
Experiments	Ref. 43	...	120
	Ref. 44	...	166
	Ref. 45	45

^aReference 2.

^bReference 6.

^cReference 14.

^dReference 21.

^eReference 24.

^fReference 42.

fault is of course still fixed by symmetry. For Al the displacement at the USFC is unchanged by relaxation. Without relaxation in the USFC the atoms in two neighboring layers are exactly superposed. If relaxation is admitted this exact superposition is avoided as long as possible. The shift of the USFC is much larger for Cu than for Al, again illustrating the much more important role of relaxation.

The inflection point on the energy vs strain curve (corresponding to the first stress maximum) for affine shear determines the ISS,⁴⁷ provided that no other instabilities occur before reaching such a large strain. Our values for the ISS of Al and Cu, together with the corresponding values of the displacement μ (or the engineering shear strain γ^E), are compiled in Table III, together with the results of previous calculations and experimental estimates. The comparison with the previous published results is difficult because the results scatter widely due to different computational methods and setups, but we note very good agreement with those of Ogata *et al.*¹⁴ Application of the alias regime of shear deformation leads to identical results for Cu, while for Al the unstable stacking fault configuration is reached at a displacement which is lower than that corresponding to the ISS.

2. Microscopic mechanism of pure alias shear deformation

The microscopic mechanism of deformation under pure alias shear strain is most directly illustrated by projecting the structure on the $(\bar{1}10)$ plane. The stacking sequence of three neighboring layers can be described by a rhombus: for the ...ABC... stacking sequence of close-packed layers in the

fcc lattice the obtuse angle of the rhombus is $\alpha=109.4^\circ$ (i.e., the ideal tetrahedral angle). If this stacking sequence is continued, all rhombi have the same shape (see Fig. 4). For the ...BCBC... stacking sequence the rhombus is replaced by a rectangle ($\alpha=90^\circ$). If an alias shear strain is applied to the top layer, its displacement induces a force on the adjacent layer which partially follows the displacement of the top layer and hence exerts force on the next layer. These displacements are visualized by a decreasing obtuse angle of the rhombi describing the stacking sequence. As long as the displacement of the top layer is only modest, this will lead to a deformation which is almost identical to that produced by a pure affine shear; i.e., the angle α will be the same in all rhombi throughout the computational cell. This homogeneous shear deformation applies almost until reaching the USFC. At a displacement of $\sim 21\%$, the angle in the two rhombi describing the stacking sequence differs only by 1.3° for Al; for Cu the difference is smaller than 1% up to the stacking fault instability. It is important to emphasize that for Al a large change in the angles of the rhombi at stacking fault formation (the angles split by 13.3°) is related to a change in energy of less than 5 meV (cf. Figs. 3 and 5). To determine the angles with an accuracy which is significantly better than 1° would require an accuracy of the total energy which must be equal to or better than 0.1 meV . This would be outrageously computationally expensive without yielding significant new information: with the present data, the onset of the stacking fault instability is determined with an accuracy which is 1% of the displacement or better. The only open question is whether a slightly inhomogeneous deforma-

TABLE III. The value of the ideal shear strength σ (in GPa) for Al and Cu under a $\langle 11\bar{2} \rangle \{111\}$ shear deformation, calculated for simple and pure affine and alias deformation. The strain at which the limiting strength is reached is given both in terms of the displacement μ (in %) and the engineering shear strain γ^E (in %) defined as $|\bar{x}|/|\text{proj}_{[111]}(\bar{c})| \times 100\%$, i.e., in terms of the relation of the displacement to the height of the computational cell.

Regime	Shear		Al			Cu		
	Mode	Source	μ	γ^E	σ	μ	γ^E	σ
Affine	Simple	This work ^a	30.0	21.2	3.82	22.7	16.0	3.41
		Ref. 48 ^g	...	20.0	3.60	...	15.7	3.48
		Ref. 49 ^b	3.00	3.16
		Refs. 15 and 20 ^b	...	21.0	3.73	...	15.7	3.43
		Ref. 14 ^b	3.71	3.45
		Ref. 14 ^c	3.83	3.61
		Refs. 11 and 30 ^d	3.40	4.00
	Pure	This work ^a	28.0	19.0	2.84	19.1	13.5	2.15
		Ref. 24 ^f	2.72
		Refs. 15 and 20 ^b	...	20.0	2.84	...	13.7	2.16
		Ref. 13 ^e	...	18.5	3.33
		Ref. 13 ^{e,h}	...	14.5	3.16
		Ref. 14 ^b	28.0	20.0	2.84	19.0	13.0	2.15
		Ref. 14 ^c	2.98	2.23
Refs. 11 and 30 ^d	...	14.5	1.85	...	13.0	2.65		
Alias	Simple	This work ^a	9.5	6.7	0.94	7.8	5.5	1.14
	Pure	This work ^a	21.0	14.5	2.60	19.6	13.7	2.11

^aGeneralized gradient approximation (GGA)-PAW.

^bGGA-US.

^cWIEN2K.

^dLocal density approximation (LDA)-Troullier-Martins (TM) or Hamann-Schlüter-Chiang (HSC) pseudopotential scheme for Cu and Al, respectively.

^eLDA-Goedecker-Teter-Hutter (GTH) pseudopotential schemes.

^fLDA.

^gGGA-US (for Al) and PAW (for Cu).

^hPhonon instability occurrence.

tion (difference in the angle of the rhombi by about 1%) precedes the formation of a stacking. This question is extremely hard to answer (it would require not only a dramatically enhanced level of convergence but also a larger supercell), and the results could not be verified experimentally. A stacking fault is created at a displacement of 21.5%: the rhombus describing the stacking of the lower three close-packed layers almost immediately recovers the ideal angle ($\alpha=109.9^\circ$), while the angle of the rhombus describing the stacking in the upper half of the cell relaxes to a smaller value, $\alpha=96.3^\circ$ (see Fig. 4). With further increasing displacement, this angle continues to decrease until at the ISFC it reaches a value of $\alpha=90^\circ$, signaling the formation of an ...ABC|BCA... stacking fault.

The variation in the angle is illustrated in the top panels of Fig. 5 for Al and Cu. For an affine shear deformation, the angle decreases linearly with the displacement. Under pure alias shear the variation is the same for Al up to 16.5% and for Cu up to 22% displacement (corresponding to 11% and 15.5% engineering strains, respectively). When a stacking fault is created, the angle undergoes a bifurcation: the angle

in the rhombus describing the ABC stacking sequence immediately returns to the ideal tetrahedral angle, while the angle in the rhombus describing the BCB stacking first decreases discontinuously by about 5° and then decreases continuously to 90° .

The deformation induced by a pure alias shear is not restricted to a relative displacement of the (111) planes; the atomic arrangement in these planes is also strongly affected. For Al and Cu, these deformations of the slip planes are very different (see Fig. 5). As already noticed by Krenn *et al.*^{30,31} and by Ogata *et al.*,¹⁴ Al is very stiff against relaxation along the $\bar{a} \equiv \langle 11\bar{2} \rangle$ direction, while for Cu the lattice parameter a contracts linearly with increasing displacement until a stacking fault is created. Along the $\bar{b} \equiv \langle 110 \rangle$ direction Al is also quite stiff, while for Cu the lattice parameter b increases. The different relaxation in the (111) plane also leads to a different variation in the interlayer distances. Shearing naturally leads to a stretching of the lattice constant c . For Al the resistance against in-plane relaxation enforces also an increase in the interlayer distance, while for Cu the distance between the close-packed layers remains unchanged. For Al, the forma-

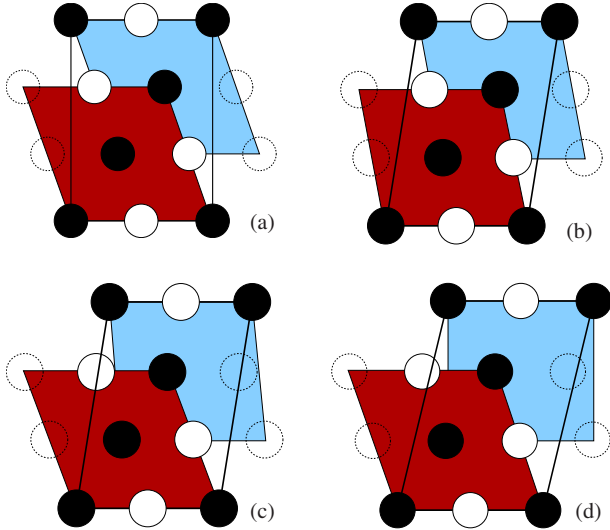


FIG. 4. (Color online) Microscopic mechanism of the $\langle 11\bar{2} \rangle \{111\}$ shear deformation of Al obtained by the alias regime. (a) Starting configuration represented by two rhombi in a $(11\bar{2})$ plane with an obtuse angle of $\alpha = 109.4^\circ$, visualizing the ideal ...ABC... stacking sequence. (b) Configuration close to the generation of a stacking fault at a displacement of 21.0%. Both rhombi have nearly identical angles of $\alpha = 102.3$ and 100.1° for the red (dark) and blue (light) rhombi, respectively. (c) Configuration immediately after formation of a stacking fault at 21.5% displacement. The red (dark) rhombus has almost completely recovered its initial shape ($\alpha = 109.9^\circ$), while the blue (light) rhombus has been transformed to another configuration ($\alpha = 96.3^\circ$). (d) The intrinsic stacking fault configuration at 33.3% displacement ($\frac{1}{6}[11\bar{2}] = \vec{b}_p$). The first (red, dark) rhombus represents the return of the lower half of the cell to the ideal ABC stacking sequence ($\alpha = 109.4^\circ$), while the second (blue, light) rhombus represents the ...BCBC...stacking fault ($\alpha = 90.0^\circ$).

tion of a stacking fault does not affect the in-plane lattice constants, while in Cu the lattice constants a and b jump back to their values in the ideal fcc lattice already at the USFC. Beyond the ISFC, the relaxation patterns are the same as for the unfaulted original structure.

Clatterbuck *et al.*¹³ demonstrated that under $\langle 11\bar{2} \rangle \{111\}$ shear deformation a phonon instability occurs at an engineering strain of 14.5%. This instability occurs at a wave vector between $\frac{1}{3}[111]$ and $\frac{1}{2}[111]$, with atomic displacements in the $[\bar{1}12]$ direction; i.e., it results in $[\bar{1}12]$ (111) shear failure with a periodicity of two or three $\{111\}$ planes. Under uniaxial $[110]$ tension a phonon instability develops at 11% engineering strain. The soft phonon has a wave vector close to $\frac{1}{3}[111]$; it corresponds to atomic displacements in the $[\bar{1}12]$ direction. Hence the failure described by the instable phonon mode is the same as that induced by the $\langle 11\bar{2} \rangle \{111\}$ shear. Clatterbuck *et al.*¹³ suggested that “this is probably because $\langle 110 \rangle$ tension can be visualized as a superposition of $\langle 11\bar{2} \rangle \{111\}$ shear and an expansion perpendicular to the shear plane.” The relation between the tensile and shear deformation modes will be discussed in detail in the following section.

3. Relation of $\langle 11\bar{2} \rangle \{111\}$ shear to uniaxial tension along the $[110]$ direction

The structure defined by the computational cell used for the modeling of the $\langle 11\bar{2} \rangle \{111\}$ shear deformation can also be described as a body-centered tetragonal (bct) lattice with space group $I4/mmm$ (139) [see Fig. 6 (left)]. The lattice parameters are given by $(b_1, b_2, b_3) = (\sqrt{2}/2, \sqrt{2}/2, 1)a^0$. They represent just another description of the fcc lattice which was used in our investigations of the response of fcc-like structures to uniaxial tensile loading along the $\langle 110 \rangle$ direction.⁵⁰ Uniaxial tensile deformation of the fcc lattice along $[110]$ corresponds to a tensile deformation of the bct cell along the lattice vector \vec{a} .

Figure 6 shows how the bct unit cell is embedded into the larger orthorhombic cell used in our simulations of the $\langle 11\bar{2} \rangle \{111\}$ shear deformation. If a $\langle 11\bar{2} \rangle \{111\}$ shear is applied to the large orthorhombic cell, this corresponds to an elongation of the lattice vector \vec{a} of the bct lattice, i.e., to a $[110]$ tensile deformation of the fcc crystal. Strictly speaking, not only the length but also the direction of the lattice vector \vec{a} are changed such that the bct cell undergoes a monoclinic deformation. However, for not too large shear deformation the relaxation of the atomic positions restores the orthogonality of the bct lattice vectors. This holds for displacements up to those where a stacking fault is generated, as shown in Fig. 6(b). After SF generation the bct cell extending on both sides of the stacking fault is severely deformed; relaxation can no longer restore the orthogonality of the lattice vectors. Seen from the point of view of a tensile deformation of the fcc lattice along the $[110]$ direction, this process illustrates the occurrence of a shear instability on the tensile deformation path.

Figure 7 shows the energy-strain curves and the variation in the lattice parameters of the bct lattice under uniaxial tension along the $[110]$ direction for Al (left panel) and Cu (right panel); for Al an extended version of these results has been published very recently.⁵⁰ Onto the energy-strain curves under tensile deformation we have mapped the appropriate energy-strain curves for shear deformation, with the strain determined according to the change in the length of the lattice vector \vec{a} of the bct lattice (note that this is possible only up to the point where a stacking fault is generated). The same definition of the strain has also been used for the mapping of the variation in the lattice parameters under tensile and shear loading. For shear deformation we have recorded the results for pure affine and pure alias shears; for tensile deformation the results for epitaxial tension (ET) [isotropic biaxial stress in the (\vec{a}, \vec{b}) plane, tetragonal symmetry] and uniaxial tension (UT) (orthorhombic deformation) are shown. For the alias regime, the mapping is valid only up to the occurrence of a SF.

For the energy-strain curves [Fig. 7(a)] we note an exact coincidence of the high-symmetry configurations (energy maximum and minimum) on the tensile and affine shear paths. The different constraints applied to the bct lattice under tensile or shear loading result in slightly different energy-strain paths at intermediate strains. The energy maximum corresponds to a metastable and stress-free bct structure with

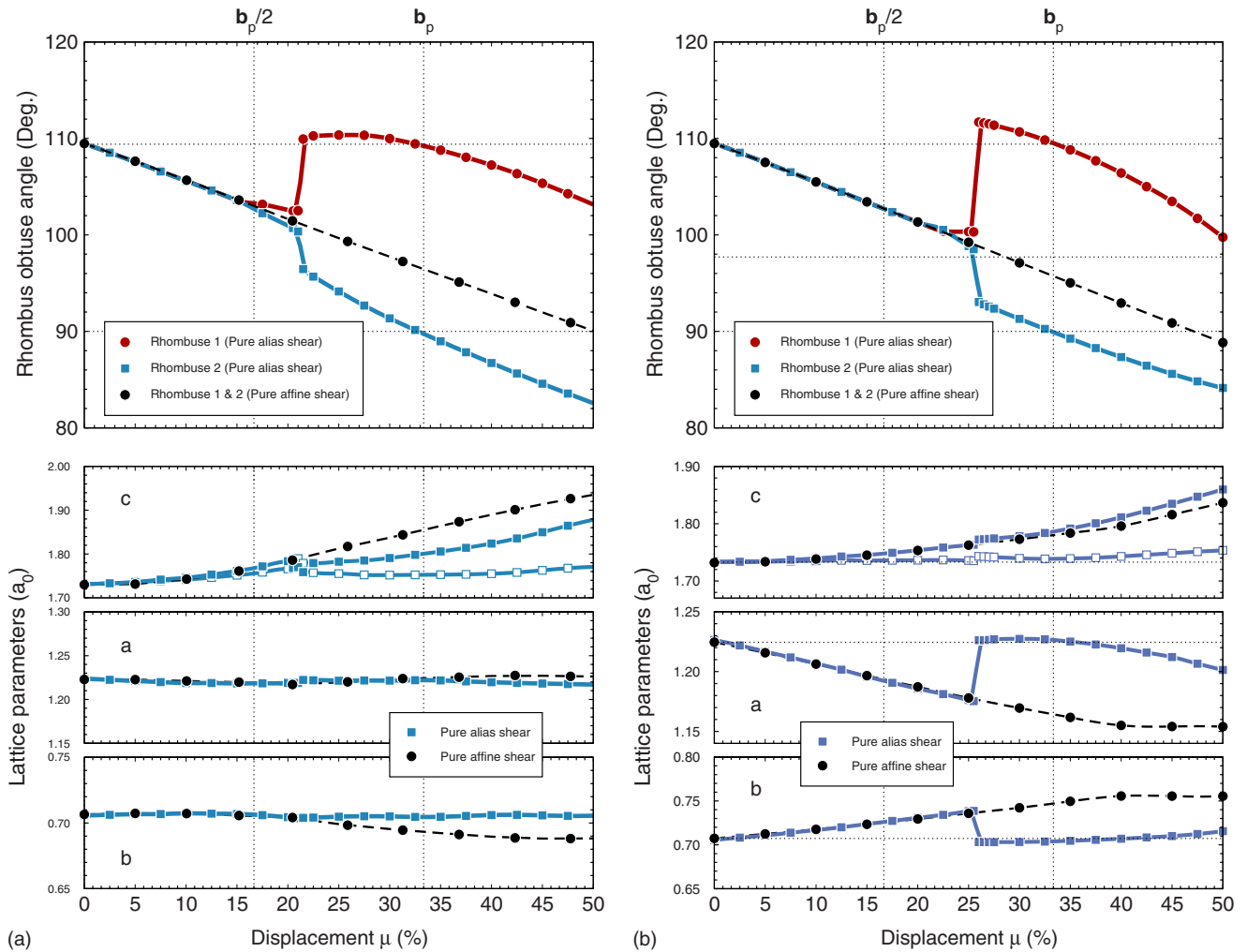


FIG. 5. (Color online) Variation in the structural parameters of fcc Al (left panel) and Cu (right panel) under $\langle 11\bar{2} \rangle \{111\}$ shear deformation. The top panel shows the variation in the obtuse angle of two rhombi characterizing the stacking sequence (see Fig. 4). The lower panels show the variation in the lattice parameters of the computational cell as a function of the displacement. The open symbols stand for the z component of \vec{c} , i.e., the height of the computational cell.

space group $I4/mmm$ (139) reached at 50.0% and 47.2% shear displacements or 22.6% and 15.0% tensile strains for Al and Cu, respectively. The close relation between these two deformation paths is evident. The close relation between shear and tensile deformations becomes even more evident if a linear transformation between shear displacement and engineering strain under tension is assumed. The scaling factors of this transformation are determined by the value of engineering tensile strain and shear displacement at the energy maximum; i.e., they are given by 22.6/50.0 for Al and 15.0/47.2 for Cu, respectively. This linear transformation also allows mapping of the alias shear beyond SF generation onto the tensile path. Figure 7(b) show that this linear transformation leads to an almost perfect coincidence of the energy/strain curves for tensile and shear deformations, especially for Al while for Cu small differences remain. This analysis shows that the generation of a stacking fault corresponds to the occurrence of a shear instability under tensile deformation at 10.0% and 8.8% strain for Al and Cu, respectively. This critical strain is in very good agreement with the results of Clatterbuck *et al.*¹³ who found a phonon instability

in Al at $\sim 11\%$ engineering tensile strain, resulting in a $[\bar{1}12]$ (111) shear failure. Our results demonstrate that a similar phonon/shear instability develops in Cu under an even lower tensile strain.

The variation in the lattice parameters under strain reveals significant differences between the relaxation processes in Al and Cu. In the previous section we have arrived at a similar conclusion: the relaxation patterns in the $\{111\}$ planes are very different: Al is very stiff, but Cu is rather soft along the $\langle 112 \rangle$ direction (parallel to the lattice vector \vec{b} common to the cell used for describing tensile and shear deformations, see Fig. 6). This can be now understood from another point of view. Figure 7(c) demonstrate that for Al, the lattice parameter b remains almost unchanged under both shear and tensile deformations up to the occurrence of the SF instability, whereas it gradually expands for Cu. The relaxation of the lattice parameter c of the bct cell under shear and uniaxial tensions is slightly different; shear deformation leads to a variation in c which is more comparable to the response to biaxial (epitaxial) tension along the $[110]$ direction. In principle this difference is understandable because this direction

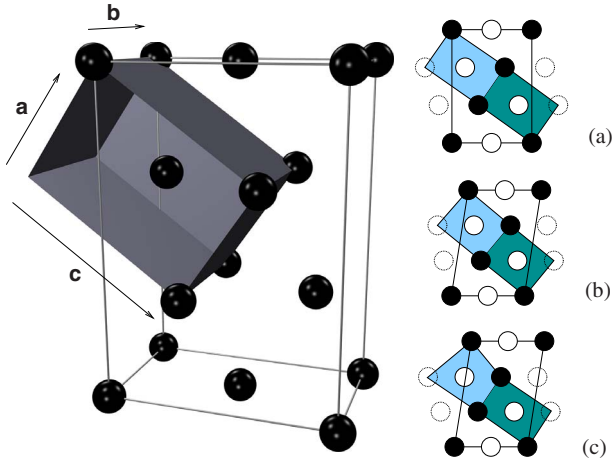


FIG. 6. (Color online) Left panel: two body-centered tetragonal cells describing an fcc lattice embedded into the large orthorhombic cell used for the modeling of a $\langle 11\bar{2} \rangle \{111\}$ shear deformation (cf. Text). The right panel shows the deformation of the bct cells under a shear deformation: (a) the starting configuration. (b) The configuration at 21.0% displacement, just before the generation of stacking fault. (c) The configuration at 21.5% displacement immediately after creation of the stacking fault.

is under compression during shear deformation causing a steeper decrease with increasing strain. This also explains the small differences in the energy-strain curves under affine shear and tensile deformations [Fig. 7(a)].

The same effect also explains that for Al the response to epitaxial and uniaxial tensile deformations is very different, while for Cu the two tensile deformation paths are much more similar. At the energy maximum along the epitaxial deformation path the symmetry is body-centered-cubic (bcc); if the volume is conserved, the bcc structure is reached at a strain of $[\sqrt[6]{2}-1] \times 100\% = 12.25\%$ and has a lattice parameter of $1/\sqrt[3]{2} \times a^0 = 0.794 \times a^0$. Due to the small volume difference between the fcc and bcc phases, the bcc structure is realized at a strain of 13.2% and 12.5% for Al and Cu, respectively. Beyond the energy maximum the energy decreases to a local minimum coincident with the local maximum along the uniaxial deformation path. The two extrema represent energetically degenerate tetragonal structures (space group $I4/mmm$, no. 139) differing in the orientation of the tetragonal axis. A tetragonal structure T_1 , with $a=c$, is realized under uniaxial tension or shear deformation, while epitaxial tension leads to a structure T_2 with $b=c$ [see Fig. 7(c)]. This indicates that the potential-energy surface is very flat at this point. For Cu, the energy difference between these tetragonal phases and the bcc structure is only about 2 meV/atom, but it is nearly 30 meV for Al. Under slightly increased uniaxial strain, phase T_1 transforms to another tetragonal phase; for details we refer to our earlier work (Ref. 50).

The important result of this comparative analysis of shearing and uniaxial tensile deformations is to demonstrate that under uniaxial tension a shear instability occurs for Al at an engineering strain of $\sim 10.0\%$ ($\sigma_{is} \sim 3.8$ GPa), lower than the strain at the ideal tensile strength of 13.6% ($\sigma_{is} = 4.2$ GPa).⁵⁰ The situation for Cu is more difficult since both mapping methods of the shearing on a tensile deforma-

tion do not work as well as for Al. Depending on the scaling, the shear instability occurs at strain of $\sim 6.2\%$ or $\sim 8.8\%$. The ideal tensile strength (ITS) under uniaxial tension along the $[110]$ direction is reached at strain of $\sim 6.2\%$ ($\sigma_{is} = 4.6$ GPa). Hence, the shear instability in Cu can coincide with the position of ITS or can be slightly beyond. However, we note again that this is just qualitative information based on our mapping methods. For Al, where the mapping works well and the SF instability occurs sufficiently before the ITS, the situation seems to be quite clear. For Cu, a final statement would be made with caution; a detailed analysis of both processes is required.

Another possible description of the change in the bct lattice is to use the length of the \bar{c} lattice vector, which is under permanent compression during the shear deformation. This process can be seen as uniaxial compression along the $[100]$ direction; a more detailed analysis will be published later.

B. $\langle \bar{1}10 \rangle \{111\}$ slip system

1. Energy- and stress-displacement curves

The energy- and stress-displacement curves obtained for Al and Cu under a $\langle \bar{1}10 \rangle \{111\}$ shear deformation are shown in Fig. 8. A detailed analysis leads to similar conclusions as for the $\langle 11\bar{2} \rangle \{111\}$ shear deformation. In the elastic region there is no difference between simple and pure, and between affine and alias shears. For larger strains, the response of Al and Cu differs substantially. While for Al the stress depends linearly on the applied strain up to displacements reaching nearly 20% (except the simple alias shear), for Cu differences between the affine and alias regimes appear already at modest displacements. Common to both metals is the identical response to pure affine and alias shears up to a displacement of $\sim 35\%$ and $\sim 41\%$ for Al and Cu, respectively. For larger strains stacking faults are created in the alias regime.

For this slip system, the formation of a stacking fault leads to a dissociation of the $\frac{1}{2}[\bar{1}10]$ dislocation into two partial Shockley dislocations. The splitting of the dissociation is caused by the possibility of forming an inequivalent stacking fault with a lower misfit energy. Figure 1(b) shows schematically this displacement path. It is evident that the shift in top layer A by 50% leads to an energetically unfavorable position; for a simple alias shear this corresponds to an energy maximum at the USFC. Upon relaxation (i.e., in the pure alias shear mode) the atoms in layer A move along the $\frac{1}{12}[\bar{1}\bar{1}2] + \frac{1}{6}[\bar{1}2\bar{1}]$ direction to a position directly above the atoms in the B layer. This results in the formation of an $\dots ABC|BCA \dots$ stacking sequence of the close-packed $\{111\}$ planes. In the pure alias shear regime the stable intrinsic stacking fault configuration (ISFC) is reached at a displacement of 50%.

The relation between the USFC and ISFC and the influence of relaxation on the location and energy of the USFC are significantly different for both slip systems. In both cases, the location of the ISFC is determined by the length of the partial Burgers vector \vec{b}_p , and this coincides for the $\langle \bar{1}10 \rangle \{111\}$ shear deformation with the USFC if relaxation is suppressed (simple alias shear). In contrast, for $\langle 11\bar{2} \rangle \{111\}$

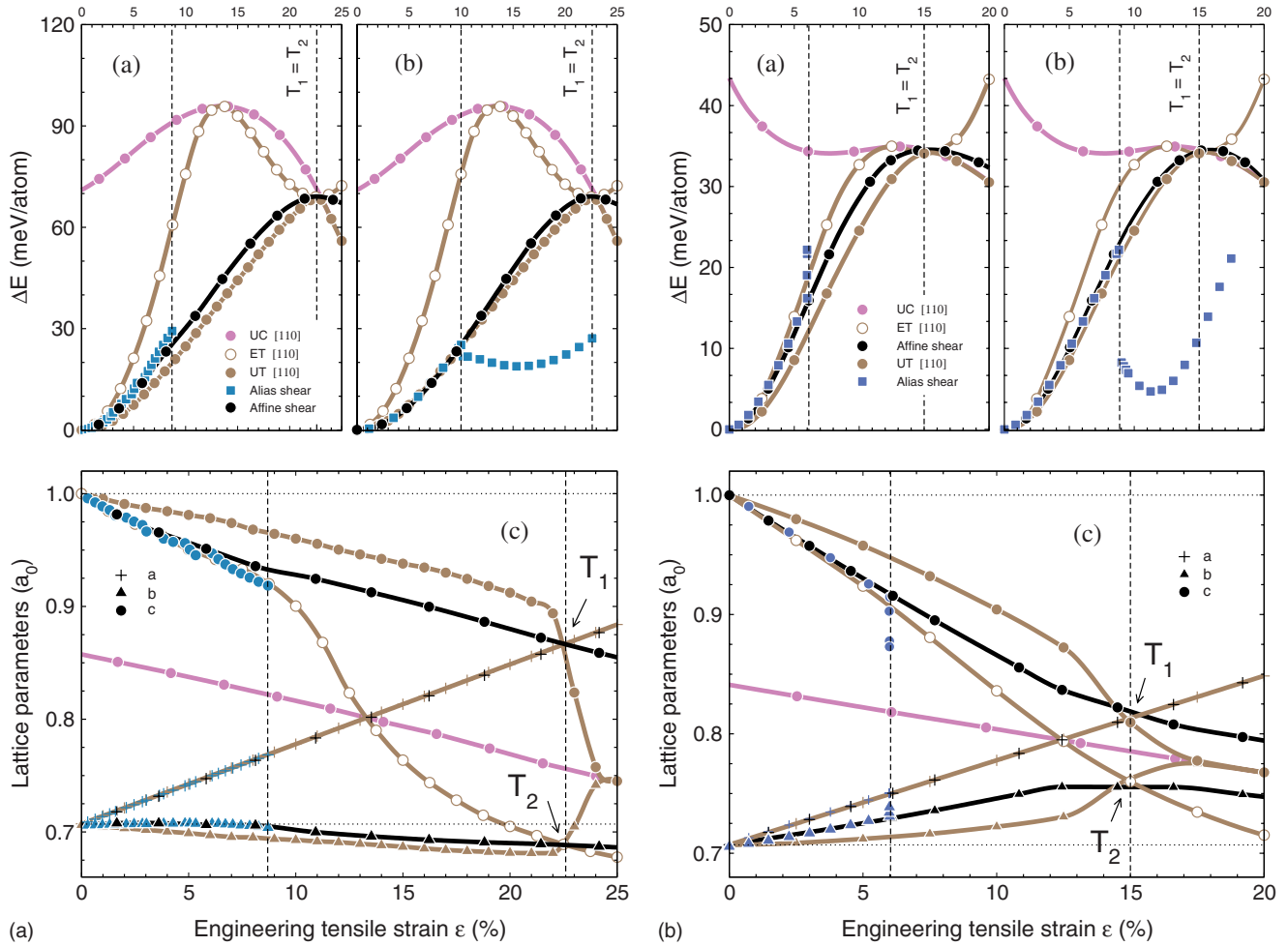


FIG. 7. (Color online) (a) and (b) The energy-strain curves and (c) the variation in the lattice parameters of the bct cell under $\langle 11\bar{2} \rangle \{111\}$ shear deformation mapped onto the results obtained for uniaxial tension along the $\langle 110 \rangle$ direction (see Ref. 50). The left side of the figure shows the results for Al; the right side shows the results for Cu. In panels (a) and (c) the displacement under tensile deformation has been measured in terms of the change in the length of the lattice vector a of bct cell; in panel (b) a linear relation between the strains under shear and tension has been assumed (cf. text). UT stands for uniaxial tension ($\epsilon = \epsilon_1$), ET stands for epitaxial tension ($\epsilon = \epsilon_1 + \epsilon_2$), and UC stands for uniaxial compression ($\epsilon = -\epsilon_1$). The vertical dashed lines indicate the strain at the USFC and at the common energy maximum under affine shear and uniaxial tensile deformations.

shear, the USFC under simple alias shear is reached at a displacement corresponding to $\sim 0.5 \rightarrow 0.6 \times \bar{b}_p$, which is equal to (for Al) or even smaller than (for Cu) the displacement at which the USFC under pure alias shear is reached. Hence for the $\langle \bar{1}10 \rangle \{111\}$ slip system relaxation has a drastic influence on the unstable stacking fault configurations and energies. From values of 503 and 735 mJ/m² calculated for simple alias shear, the stacking fault energy is reduced to 226 and 196 mJ/m² under pure alias shear for Al and Cu, respectively. The USFC is also reached at much smaller displacements, at $\sim 35\%$ and $\sim 41\%$ for Al and Cu, respectively, if relaxation is admitted (see Table IV). In contrast, the position of ISFC is fixed at $\bar{b}_p = \frac{1}{2}[\bar{1}10]a_0$ and the intrinsic stacking fault energy necessarily agrees with the value calculated for $\langle 11\bar{2} \rangle \{111\}$ shear deformation, i.e., 126 and 37 meV for Al and Cu, respectively. Due to the splitting of the dislocation into two Shockley partials, the $\langle \bar{1}10 \rangle \{111\}$ shear deformation leads to the same ISFC than a $\langle 11\bar{2} \rangle \{111\}$ shear

deformation—in agreement with experimental observations. The energy-displacement profiles for the $\langle \bar{1}10 \rangle \{111\}$ and $\langle 11\bar{2} \rangle \{111\}$ slip systems can be mapped onto each other if the initial and ISF configurations are matched. The profiles for $\langle 11\bar{2} \rangle \{111\}$ shear are superposed in Fig. 8 to those under the $\langle \bar{1}10 \rangle \{111\}$ shear (open symbols). The comparison shows that under the $\langle 11\bar{2} \rangle \{111\}$ shear the instability under pure alias shear is always reached at a smaller displacement than under the $\langle \bar{1}10 \rangle \{111\}$ shear and followed by a more pronounced relaxation after slip. The important point is that the energy maxima (i.e., the USF energies under pure alias shear) are almost the same for both slip systems (the difference is slightly larger for Al than for Cu); this indicates that both mechanisms for the formation of a stacking fault can coexist. However, for a $\langle 11\bar{2} \rangle \{111\}$ shear deformation, the stacking fault is generated already at a smaller displacement $|\bar{b}_p^{(11\bar{2})}| = \sqrt{6}/6 \times a_0$ and $|\bar{b}_p^{(\bar{1}10)}| = \sqrt{2}/2 \times a_0$.

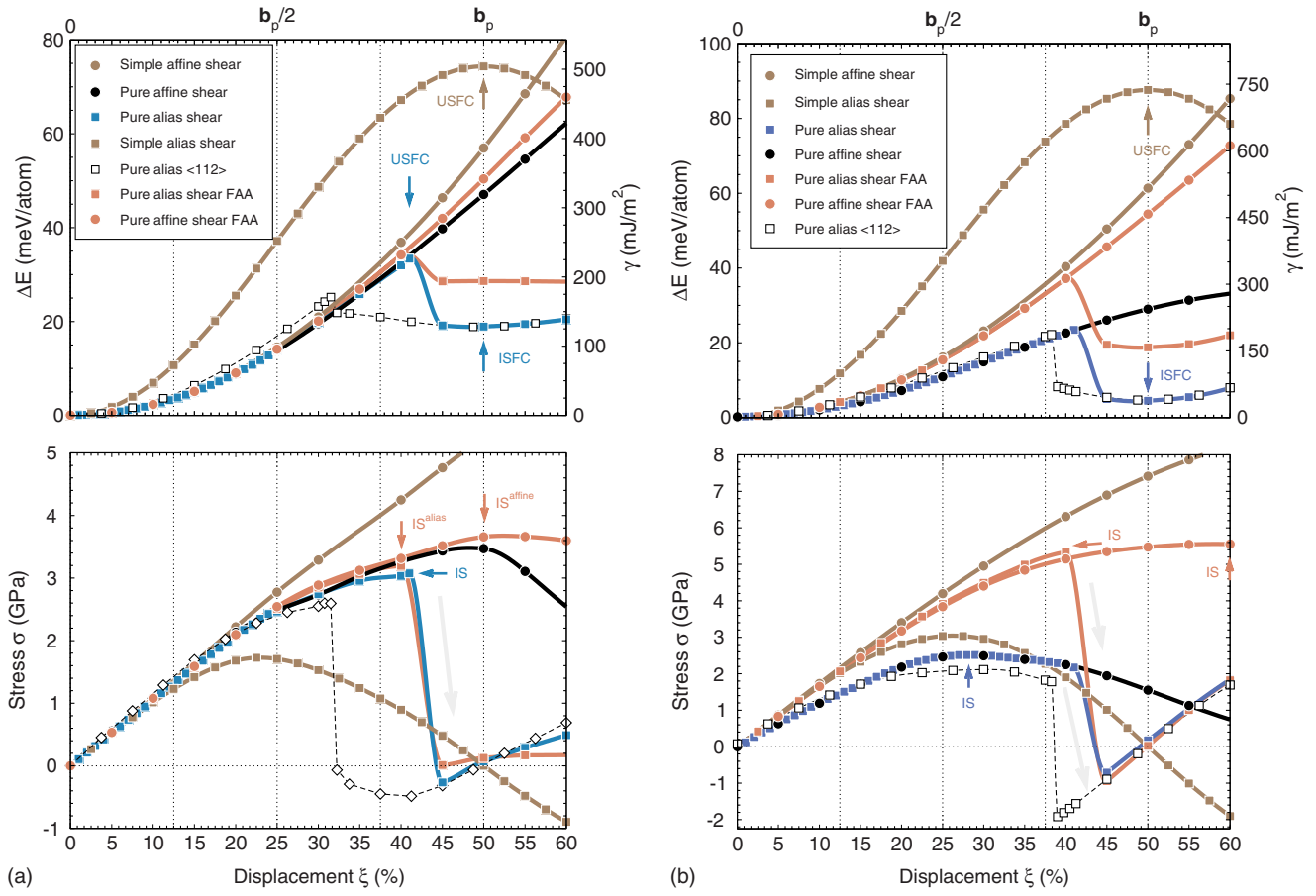


FIG. 8. (Color online) Energy- and stress-displacement curves under a $\langle \bar{1}10 \rangle \{111\}$ shear deformation for Al (left) and Cu (right), calculated for different deformation modes. The labels IS, USFC, and ISFC mark the ideal strength, unstable, and intrinsic stacking fault configurations. The dashed lines show for comparison the energy- and strain-displacement curves calculated for $\langle 11\bar{2} \rangle \{111\}$ shear (cf. text). The abbreviation FAA (fixed all angles) denotes curves where all lateral shifts are suppressed and where the angles of the computational cell are kept constant.

The ideal strength is defined by the stress maximum (or the inflection point on the energy-displacement curves); the values are collected in Table V. We note a substantial difference between Al and Cu. For Al under alias shear, a stacking fault is generated before the stress maximum under pure affine shear is reached; the ideal shear strength is reduced from 3.47 GPa at 50% displacement to 3.07 GPa at 41%. The shear strength is even much lower under simple alias shear. In contrast for Cu the stress maximum is reached before a stacking fault is generated, the ideal strength is exactly the same under pure affine and alias shears (see Table V), it is

only slightly lower than under simple alias shear. The ideal strength under $\langle \bar{1}10 \rangle \{111\}$ shear is higher by about 20% than under the $\langle 11\bar{2} \rangle \{111\}$ shear if relaxation is allowed (cf. Tables III and V).

Finally, we note the extreme importance of relaxation for this shear system, especially for Cu. As will be discussed in more detail in the next subsection, both alias and affine shears lead to large changes in the volume and shape of the unit cell. Figure 8 shows for comparison the energy-displacement and stress-displacement curves (denoted as FAA) where during the relaxation all lateral shifts are sup-

TABLE IV. Stacking fault energies (in mJ/m²) for Al and Cu for $\langle \bar{1}10 \rangle \{111\}$ shear deformation.

		Al		Cu	
Data source		γ_{usf}	γ_{isf}	γ_{usf}	γ_{isf}
This work	Simple alias shear	503	...	735	...
	Pure alias shear	226	126	196	37
	Pure alias shear (FAA)	234	191	313	156
Others	(LDA) ^a	250

^aReference 46.

TABLE V. The value of the ideal strength σ (in GPa) for Al and Cu for $\langle\bar{1}10\rangle\{111\}$ shear deformation. The position of σ can be represented as value of displacement ξ (in %) or engineering shear strain γ^E (in %) defined as $|\bar{x}|/|\text{proj}_{[111]}(\bar{c})|\times 100\%$, i.e., division of the displacement and height of the computational cell.

Regime	Shear		Al			Cu		
	Mode	Source	ξ	γ^E	σ	ξ	γ^E	σ
Affine	Simple	This work ^a
		Ref. 49 ^b	3.77	5.90
	Pure	This work ^a	50.0	20.4	3.47	28.0	11.4	2.51
Alias	Pure (FAA)	This work ^a	50.0	20.4	3.64	60.0	24.5	5.55
	Simple	This work ^a	22.5	9.2	1.73	26.0	10.5	3.04
	Pure	This work ^a	41.0	16.7	3.07	28.0	11.4	2.51
	Pure (FAA)	This work ^a	40.0	16.3	3.21	40.0	16.3	5.34

^aGGA-PAW.

^bGGA-US.

pressed and where the angles of the computational cell are kept constant. This implies that there are no atomic rearrangements in the basal plane. This restricted relaxation leads to a large increase in energy and strain; the profiles are similar to those for a simple alias shear nearly up to the generation of a stacking fault.

2. Microscopic mechanism of alias pure shear

The microscopic mechanism for a $\langle\bar{1}10\rangle\{111\}$ shear deformation differs in characteristic aspects from that under a $\langle 11\bar{2}\rangle\{111\}$ shear. Figure 9 shows the displacements of the atoms in the A, B, and C layers during the $\langle\bar{1}10\rangle\{111\}$ shear deformation. The small black circles indicate the actual positions at each step of displacement after a full relaxation. Initially the displacement of the A atoms follows the $[\bar{1}10]$ direction of the applied shear strain indicated by the arrow. The shift in the A layer also induces a smaller shift in the underlying C and B layers. At a sufficiently large displacement

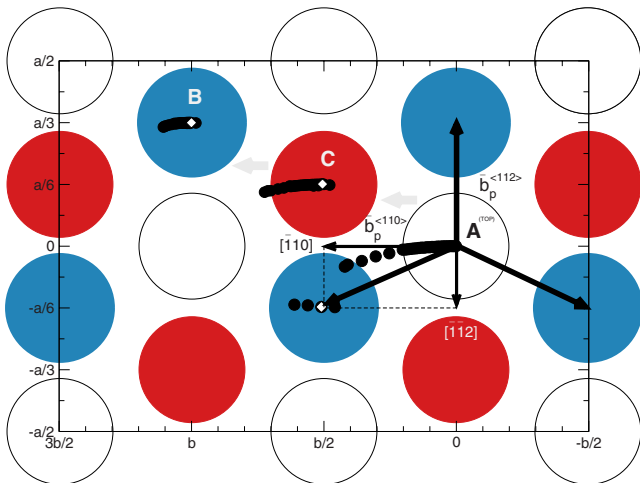


FIG. 9. (Color online) Displacement of the atoms in the A, B, and C $\{111\}$ layers of fcc Al under a pure alias $\langle\bar{1}10\rangle\{111\}$ shear (cf. text).

ment a repulsive interaction between the A atoms and those in the C layer begins to be felt. Due to this repulsive interaction the displacement of the A atoms develops a component along the $[\bar{1}\bar{1}2]$ direction. The A atoms approach a position above the atoms in the B layer. The atoms in the C and B layers follow the displacement of the A atoms with a reduced amplitude. Under increasing strain the displacements increase until the unstable stacking fault configuration is reached. At this point the A atoms jump to a position above the atoms in the B layer; but because these atoms have also been displaced in the $[\bar{1}10]$ direction, the position of the A atoms immediately after stacking fault generation is displaced from the ideal stacking position. The relaxation under further increasing strain brings the atoms in all layers back to their ideal sites in the ISFC (marked by white diamonds in Fig. 9).

The position of the atoms in the A layer can be described as $\vec{P} = \vec{P}(\mu, \xi) = \mu \vec{b}_p^{(112)} + \xi \vec{b}_p^{(\bar{1}10)}$, i.e., as a superposition of the displacements in the two orthogonal directions $[\bar{1}10]$ and $[\bar{1}\bar{1}2]$. If $\mu=0$, the A atoms are shifted only in the direction of the applied shear strain; i.e., the influence of the repulsive interactions with the C atoms is ignored, e.g., by applying an additional constraint (fixed angles of the computational cell). The energy- and stress-displacement curves computed under this constraint are presented in Fig. 8. It is evident that this constraint leads to a strong increase in energy and stress at a fixed displacement, approaching the values calculated for simple affine shear.

The second limiting case is described by $\mu = -\xi$; i.e., the displacement of the A atoms under $\langle\bar{1}10\rangle\{111\}$ shear is fully redirected into the $[\bar{1}2\bar{1}]$ direction because of a very strong repulsive interaction even at small strain. The stronger the repulsive interaction, the more the atomistic displacement patterns under $\langle\bar{1}10\rangle\{111\}$ and $\langle 11\bar{2}\rangle\{111\}$ shear deformations will be similar.

The common feature of both slip systems is the ISFC formed at $\vec{P}(-\frac{1}{2}, 1) = -\frac{1}{2}\vec{b}_p^{(112)} + \vec{b}_p^{(\bar{1}10)} = \frac{1}{12}[\bar{1}\bar{1}2] + \frac{1}{6}[\bar{1}2\bar{1}] = \frac{1}{4}[\bar{1}10]$. This decomposition of the displacement vector of

the A atoms describes the splitting the dislocation into two Shockley partials. For the ISFC the positions of the atoms in the A, B, and C planes are marked by white diamonds in Fig. 9. This demonstrates that after a large displacement from their ideal positions at intermediate strain, the atoms in the C and B layers return to their ideal positions after stacking fault generation and full relaxation. The state of maximal distortion is very close to the USFC; the values of μ for atoms in the A, C, and B layers are $(-0.33/-0.13/-0.09)$ and $(-0.62/-0.25/0.01)$ for Al and Cu, respectively. The corresponding values of ξ (measuring the displacement in the direction of the applied shear strain) are $(0.84/0.45/0.21)$ and $(0.87/0.48/0.23)$. Al and Cu differ mostly in the values of μ ; i.e., because of a stronger repulsive interaction the atoms in the top A layer of Cu are much more redirected to move along the $[\bar{1}2\bar{1}]$ direction. The displacement of the atoms in the A layer up to SF generation is described by $\mu_{\text{Al}}^A \approx 0.05\xi - 0.52\xi^2$ for Al and by $\mu_{\text{Cu}}^A \approx -0.29\xi - 0.54\xi^2$ for Cu. The important difference is seen in the linear term; at small displacements the Al atoms move essentially in the direction of the applied strain, while the Cu are already pushed toward the $[\bar{1}2\bar{1}]$ direction. This is also reflected in the change in the cell shape under applied shear strain (see below). The different response of both metals is also reflected in the propagation of the displacement from the top to the underlying layers; the displacement amplitude of the C layer is almost twice as large for Cu than for Al, but the B layer is displaced only for Al, while it remains almost stationary for Cu (see the values of μ at the USFC).

The ISFC can be represented in a similar way as for a $\langle 11\bar{2} \rangle \{111\}$ shear deformation where we have described the variation in the stacking of the close-packed layers in terms of two interpenetrating rhombi. For a fcc stacking sequence the obtuse angle of the rhombus is 109.5° , while for a hcp stacking sequence it becomes 90° (see Fig. 4). These rhombi are in fact projections of parallelepipeds onto the $(11\bar{2})$ plane. Under the $\langle 11\bar{2} \rangle \{111\}$ shear deformation the obtuse angles of these rhombi first decrease continuously, while at stacking fault generation a discontinuous change takes place; upon relaxation the angle describing the stacking fault approaches 90° , while that describing the stacking of the underlayers returns to its initial value. Under a $\langle 1\bar{1}0 \rangle \{111\}$ shear deformation the two parallelepipeds are not only sheared but also displaced in the $[11\bar{2}]$ direction. The combined change due to shearing and lateral displacement is visualized in Fig. 10 for the ISFC (which agree for both slip systems).

The development of the lattice parameters of the computational cell under increasing strain is shown in Fig. 11. This is further illustration of the difference in the response of Al and Cu to shear loading. Under the $\langle 11\bar{2} \rangle \{111\}$ shear deformation the shape of the cell is monoclinic at all displacements; under the $\langle \bar{1}10 \rangle \{111\}$ shear the symmetry is reduced to triclinic. The angle α increases linearly with the displacement under both affine and alias shears. For Al, the angles β and γ undergo only small variations up to stacking fault generation, while for Cu β increases and γ decreases. For Al, the in-plane lattice constants a and b remain almost unchanged, while for Cu a increases, while b decreases with

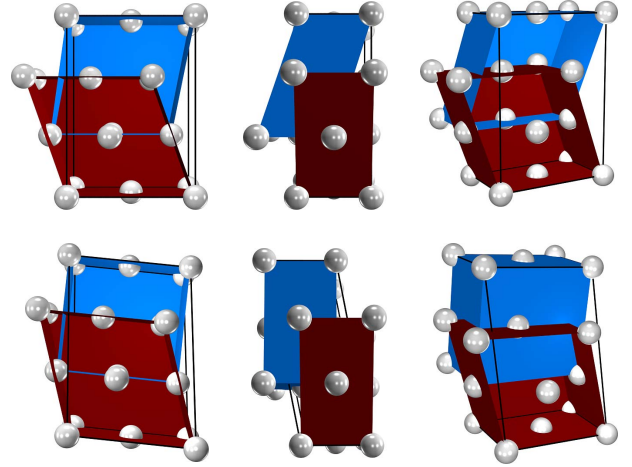


FIG. 10. (Color online) Arrangement of the atoms in the computational cell at 0% (top row) and 50% (bottom row) displacement under a $\langle 1\bar{1}0 \rangle \{111\}$ shear deformation. This configuration corresponds to another representation of the intrinsic stacking fault configuration under $\langle 11\bar{2} \rangle \{111\}$ shear deformation (cf. Fig. 4). The stacking sequence in triplets of close-packed planes is represented by two interpenetrating parallelepipeds viewed under different angles (cf. Text).

the applied strain. The response to affine and alias shears is identical almost up to the USFC. The results illustrate that in-plane relaxation is strong for Cu and modest for Al (as already discussed above). Due to the much higher stiffness of Al against in-plane distortions, the lattice constant c increases much more strongly for Al than for Cu.

IV. DISCUSSION AND CONCLUSION

We have used *ab initio* density-functional calculations to investigate the response of two fcc metals, Al and Cu, to shear deformation parallel to the close-packed (111) planes along the $[11\bar{2}]$ and $[\bar{1}10]$ directions. The simulations were based on periodically repeated cells (i.e., having no free surface) consisting of three (111) fcc layers. Two different regimes of shear deformation have been considered: affine shear where the crystal undergoes a homogeneous deformation of the lattice, and alias shear where only the top layer of the computational cell is displaced and the deformation propagates through the crystal due to the interaction between the atoms in adjacent layers. The alias regime provides a more realistic description of the shear deformation where an external strain is applied to the top layer of a sample. In addition, the alias regime allows the formation of stacking faults such that shear deformation, theoretical shear strength, and stacking fault formation can be discussed on a common footing. In both the affine and alias regimes, studies for simple and pure shear deformations (as defined by Ogata *et al.*¹⁴) have been considered. Simple shear means that relaxation of the shape of the computational cell and of the internal coordinates of the atoms after each deformation step is excluded, while pure shear implies a full relaxation such that all elements of the stress tensor except σ_{13} (for $\langle 11\bar{2} \rangle \{111\}$

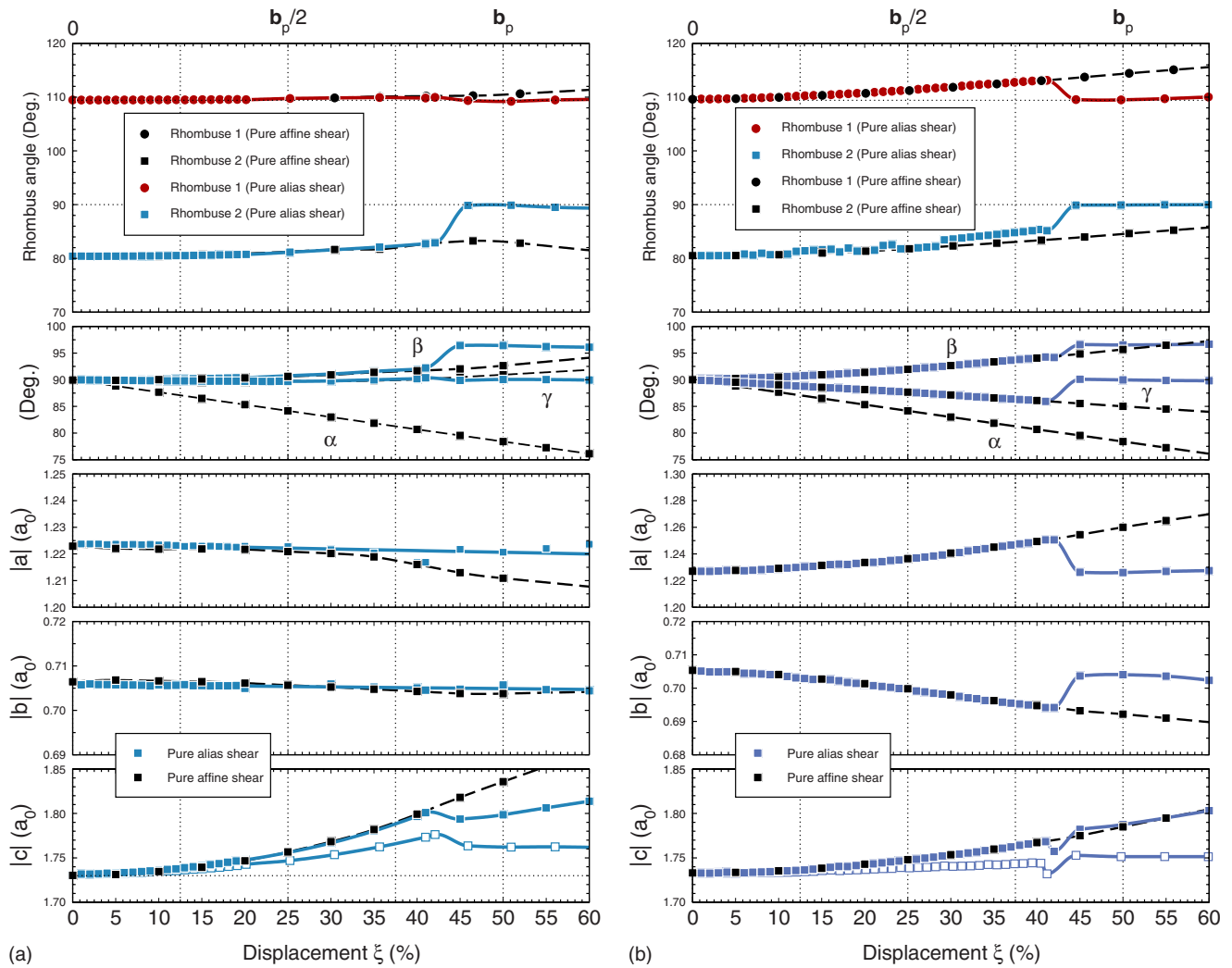


FIG. 11. (Color online) Variation in the shape of the computational cell for Al (left panels) and Cu (right panels) under the $\langle \bar{1}10 \rangle \{111\}$ shear deformation. The top panels show the variation in the obtuse angles of the two rhombi used to describe the stacking of the close-packed planes (cf. Fig. 10 and text). The lower panels show the variation in the lattice parameters a , b , and c and of the angles α , β , and γ of the computational cell as a function of the displacement under the $\langle \bar{1}10 \rangle \{111\}$ shear deformation. The open symbols show the variation in the z component of \bar{c} , i.e., of the height of the computational cell (cf. Text).

shear deformation) or σ_{23} (for $\langle \bar{1}10 \rangle \{111\}$ shear) vanish. The differences in the shear deformation between the two metals due to the different character of the interatomic interactions in the simple metal Al and in the noble metal Cu are most evident in the pure alias regime.

In the elastic limit, i.e., for small applied strains, pure affine and alias deformations lead to similar energy-strain and stress-strain curves, but for larger strain the distinction between both regimes becomes crucial. Simulations in the pure alias mode demonstrate that for both slip systems in Al the unstable stacking configurations are reached before the stress maximum; i.e., the theoretical shear strength of Al is limited by stacking fault formation. For Cu, the strain corresponding to the theoretical shear strength is smaller than the unstable stacking fault configuration. For both metals the ideal strength is higher by about 20% under $\langle \bar{1}10 \rangle \{111\}$ than under $\langle 11\bar{2} \rangle \{111\}$ shear if the system is allowed to relax. The ideal shear strength of Al is higher than for Cu—in contrast

to the much higher shear moduli of this metal.

Under the $\langle \bar{1}10 \rangle \{111\}$ shear the analysis of the atomistic deformation mechanism shows that in this case the formation of a stacking fault leads to a splitting of the $\frac{1}{2}[\bar{1}10]$ dislocation into two partial Shockley dislocations. Due to the repulsive interaction between the atoms in adjacent close-packed planes, the atoms in the top A layer move along $\frac{1}{12}[\bar{1}\bar{1}2] + \frac{1}{6}[\bar{1}2\bar{1}]$ to a position directly above the B layer such that the stable intrinsic stacking fault configuration is the same for both slip systems.

For both slip systems, the analysis of the variation in the lattice parameters under strain reveals significant differences in the relaxation behavior of both metals: Al is very stiff, but Cu is rather soft along $[11\bar{2}]$; in-plane relaxation is very strong for Cu but modest for Al. This much stronger relaxation explains that while the differences in the unstable stacking fault energies of both metals are only modest, the intrinsic stacking fault energies differ by as much as a factor

of 4. Interesting conclusions can also be derived from the comparison of the energy-strain curves under the $\langle 11\bar{2} \rangle \{111\}$ shear deformation and uniaxial or epitaxial tensile deformation along the $[110]$ direction. It was shown that the energy-strain curves for tensile and shear deformations can be mapped on each other, demonstrating that the generation of a stacking fault corresponds to the occurrence of a shear instability under tensile deformation at a critical strain, in agreement with the finding of Clatterbuck *et al.*¹³ reporting a phonon instability under tensile strain resulting in shear failure.

The differences observed in the theoretical strength and stacking fault energies, as well as the differences in the relaxation behavior, are directly related to the bonding properties of Al and Cu. These differences are correctly described by density-functional calculations which account correctly

for all relevant bonding effects (s - d hybridization in Cu, many-electron effects in Al, etc.). The success of the present study opens the way to *ab initio* investigations of shear deformations in transition-metal compounds, where covalent bonding effects prevent a description in terms of classical force fields, as demonstrated by our investigations of tensile loading.⁵¹

ACKNOWLEDGMENTS

Work at the University of Vienna has been supported by the VASP project and within the University Research Focus “Material Science” and “Computational Science.” We thank T. Bučko for provision of GADGET structural optimization package.

*michal.jahnatek@univie.ac.at

†juergen.hafner@univie.ac.at

‡marian.krajci@savba.sk

- ¹J. Pokluda, M. Černý, P. Šandera, and M. Šob, *J. Comput.-Aided Mater. Des.* **11**, 1 (2004).
- ²C. Woodward, D. R. Trinkle, L. G. Hector, Jr., and D. L. Olmsted, *Phys. Rev. Lett.* **100**, 045507 (2008).
- ³A. Kelly, W. R. Tyson, and A. H. Cottrell, *Philos. Mag.* **15**, 567 (1967).
- ⁴J. P. Hirth and J. Lothe, *Theory of Dislocations*, 2nd ed. (John Wiley & Sons, New York, 1982).
- ⁵S. G. Srinivasan, X. Z. Liao, M. I. Baskes, R. J. McCabe, Y. H. Zhao, and Y. T. Zhu, *Phys. Rev. Lett.* **94**, 125502 (2005).
- ⁶S. Kibey, J. Liu, D. Johnson, and H. Sehitoglu, *Acta Mater.* **55**, 6843 (2007).
- ⁷L. Lu, Y. Shen, X. Chen, L. Qian, and K. Lu, *Science* **304**, 422 (2004).
- ⁸M. Chen, E. Ma, K. J. Hemker, H. Sheng, Y. Wang, and X. Cheng, *Science* **300**, 1275 (2003).
- ⁹X. Z. Liao, F. Zhou, E. J. Lavernia, S. G. Srinivasan, M. I. Baskes, D. W. He, and Y. T. Zhu, *Appl. Phys. Lett.* **83**, 632 (2003).
- ¹⁰H. Rösner, J. Markmann, and J. Weissmüller, *Philos. Mag. Lett.* **84**, 321 (2004).
- ¹¹D. Roundy, C. R. Krenn, M. L. Cohen, and J. W. Morris, Jr., *Phys. Rev. Lett.* **82**, 2713 (1999).
- ¹²W. Luo, D. Roundy, M. L. Cohen, and J. W. Morris, Jr., *Phys. Rev. B* **66**, 094110 (2002).
- ¹³D. M. Clatterbuck, C. R. Krenn, M. L. Cohen, and J. W. Morris, Jr., *Phys. Rev. Lett.* **91**, 135501 (2003).
- ¹⁴S. Ogata, J. Li, and S. Yip, *Science* **298**, 807 (2002).
- ¹⁵S. Ogata, J. Li, N. Hirotsaki, Y. Shibutani, and S. Yip, *Phys. Rev. B* **70**, 104104 (2004).
- ¹⁶Y.-L. Liu, Y. Zhang, H.-B. Zhou, G.-H. Lu, and M. Kohyama, *J. Phys.: Condens. Matter* **20**, 335216 (2008).
- ¹⁷J. A. Zimmerman, H. Gao, and F. F. Abraham, *Modell. Simul. Mater. Sci. Eng.* **8**, 103 (2000).
- ¹⁸N. Kioussis, M. Herbranson, E. Collins, and M. E. Eberhart, *Phys. Rev. Lett.* **88**, 125501 (2002).
- ¹⁹R. D. Boyer, J. L., S. Ogata, and S. Yip, *Modell. Simul. Mater.*

Sci. Eng. **12**, 1017 (2004).

- ²⁰S. Ogata, J. Li, and S. Yip, *Phys. Rev. B* **71**, 224102 (2005).
- ²¹C. Brandl, P. M. Derlet, and H. VanSwygenhoven, *Phys. Rev. B* **76**, 054124 (2007).
- ²²V. Vitek, *Phys. Status Solidi* **18**, 687 (1966).
- ²³V. Vitek, *Philos. Mag.* **18**, 773 (1968).
- ²⁴D. Finkenstadt and D. D. Johnson, *Phys. Rev. B* **73**, 024101 (2006).
- ²⁵G. Kresse and J. Furthmüller, *Comput. Mater. Sci.* **6**, 15 (1996).
- ²⁶G. Kresse and J. Furthmüller, *Phys. Rev. B* **54**, 11169 (1996).
- ²⁷J. P. Perdew, J. A. Chevary, S. H. Vosko, K. A. Jackson, M. R. Pederson, D. J. Singh, and C. Fiolhais, *Phys. Rev. B* **46**, 6671 (1992).
- ²⁸P. E. Blöchl, *Phys. Rev. B* **50**, 17953 (1994).
- ²⁹G. Kresse and D. Joubert, *Phys. Rev. B* **59**, 1758 (1999).
- ³⁰C. R. Krenn, Ph.D. thesis, Ernest Orlando Lawrence Berkeley National Laboratory, 2000.
- ³¹C. R. Krenn, D. Roundy, J. W. Morris, Jr., and M. L. Cohen, *Mater. Sci. Eng., A* **317**, 44 (2001).
- ³²B. Eisenmann and H. Schäfer, *Elements, Borides, Carbides, Hydrides* Landolt-Börnstein, New Series, Group III, Condensed Matter, Vol. 14a (Springer-Verlag, Berlin, 1988), pp. 12–23.
- ³³A. G. Every and A. K. McCurdy, *Second and Higher Order Elastic Constants* Landolt-Börnstein, New Series, Group III, Condensed Matter, Vol. 29a (Springer-Verlag, Berlin, 1992), pp. 159–172.
- ³⁴H. J. Monkhorst and J. D. Pack, *Phys. Rev. B* **13**, 5188 (1976).
- ³⁵M. Methfessel and A. T. Paxton, *Phys. Rev. B* **40**, 3616 (1989).
- ³⁶P. E. Blöchl, O. Jepsen, and O. K. Andersen, *Phys. Rev. B* **49**, 16223 (1994).
- ³⁷T. Bučko, J. Hafner, and J. G. Ángyán, *J. Chem. Phys.* **122**, 124508 (2005).
- ³⁸R. P. Feynman, *Phys. Rev.* **56**, 340 (1939).
- ³⁹O. H. Nielsen and R. M. Martin, *Phys. Rev. Lett.* **50**, 697 (1983).
- ⁴⁰O. H. Nielsen and R. M. Martin, *Phys. Rev. B* **32**, 3780 (1985).
- ⁴¹N. Bernstein and E. B. Tadmor, *Phys. Rev. B* **69**, 094116 (2004).
- ⁴²S. Kibey, J. B. Liu, D. D. Johansson, and H. Sehitoglu, *Appl. Phys. Lett.* **89**, 191911 (2006).
- ⁴³R. H. Rautioaho, *Phys. Status Solidi B* **112**, 83 (1982).

- ⁴⁴L. Murr, *Interfacial Phenomena in Metals and Alloys* (Addison-Wesley Publishing Co., India, 1975).
- ⁴⁵C. B. Carter and I. L. F. Ray, *Philos. Mag.* **35**, 189 (1977).
- ⁴⁶G. Lu, N. Kioussis, V. V. Bulatov, and E. Kaxiras, *Phys. Rev. B* **62**, 3099 (2000).
- ⁴⁷F. Milstein, *Phys. Rev. B* **3**, 1130 (1971).
- ⁴⁸S. Kamran, K. Chen, and L. Chen, *Phys. Rev. B* **79**, 024106 (2009).
- ⁴⁹M. Černý and J. Pokluda, *Mater. Sci. Eng., A* **483-484**, 692 (2008).
- ⁵⁰M. Jahnátek, M. Krajčí, and J. Hafner, *Phys. Rev. B* **76**, 014110 (2007).
- ⁵¹M. Jahnátek, M. Krajčí, and J. Hafner, *Phys. Rev. B* **71**, 024101 (2005).